Journal of Applied Data Sciences
Vol. 7, No. 3, September 2026, pp. 2161-2174

Lion-Optimized ANFIS Control for a Hybrid PV–Wind–Battery System with a Reduced-Switch 31-Level Inverter for Induction Motor Drives

R K Padmashini[1,*], D Lakshmi[2], J N Rajesh Kumar[3], C N Ravi[4], P Jeyarani[5]

[1,2]Dept. of Electrical and Electronics Engineering, AMET University, Chennai-603102, India

[3]Department of CSE Sree Sastha Institute of Engineering and Technology, India

[4]Vidya Jyothi Institute of Technology, Hyderabad, India

[5]Centre for Data Science and Sustainable Technologies, INTI International University, Nilai, N. Sembilan, Malaysia

(Received: January 15, 2026; Revised: March 20, 2026; Accepted: June 25, 2026; Available online: August 9, 2026)

Abstract

This study proposes and experimentally validates a hybrid photovoltaic–wind–battery energy conversion system for driving a three-phase induction motor under variable renewable-source conditions. The system integrates a high-gain SEPIC converter, a PWM rectifier, a bidirectional battery converter, a reduced-switch 31-level cascaded H-bridge inverter, and a Lion Optimization Algorithm–tuned adaptive neuro-fuzzy inference system controller. The proposed controller performs maximum power point tracking and regulates the common DC-link voltage by adjusting the converter and rectifier switching commands in response to changes in solar irradiance, photovoltaic temperature, and wind-side voltage. The system was evaluated using MATLAB/Simulink and an FPGA-based experimental prototype. The photovoltaic array produced approximately 134 V and 75 A under the tested operating conditions, while the SEPIC converter and PWM rectifier maintained the DC-link voltage near 400 V. The battery state of charge remained around 60%, indicating balanced charging and discharging operation. The 31-level inverter generated a stable multilevel output with an RMS voltage of approximately 499 V and real power of approximately 4990 W. The simulated total harmonic distortion was 1.39%, while the experimental prototype achieved 2.85%. The experimental results were consistent with the simulation outcomes and confirmed the effectiveness of the proposed controller in improving transient response, reducing steady-state fluctuations, and maintaining stable power delivery to the induction motor. The proposed configuration provides a feasible solution for renewable-powered motor-drive and marine propulsion applications requiring high voltage gain, adaptive control, energy-storage coordination, and low harmonic distortion.

Keywords: Adaptive Neuro-Fuzzy Inference System, Battery Energy Storage, Cascaded H-Bridge Inverter, High-Gain SEPIC Converter, Hybrid Renewable Energy System, Induction Motor Drive, Lion Optimization Algorithm, Maximum Power Point Tracking, Photovoltaic–Wind System, Total Harmonic Distortion, Process Innovation.

1. Introduction

The transition toward low-emission marine transportation has accelerated the development of hybrid electric propulsion systems supplied by renewable energy sources. Photovoltaic (PV) and wind energy conversion systems (WECS) offer a practical pathway for reducing fuel consumption and emissions in marine vessels; however, their power outputs are inherently intermittent and strongly influenced by irradiance, temperature, wind speed, and operating conditions. In wind-based generation, disturbances in the grid and variations in aerodynamic input can significantly affect the voltage, power, and dynamic stability of doubly fed induction generator systems [1], [2]. Similar reliability challenges occur in grid-connected PV systems, where uncertain generation and changing environmental conditions require coordinated sizing, conversion, storage, and control strategies [3].

Energy storage is therefore essential for maintaining the continuity and stability of a hybrid renewable propulsion system. Batteries can compensate for short-term power deficits, absorb excess renewable energy, and support the DC-link voltage during rapid source and load variations. Hybrid storage configurations have also been shown to improve

*Corresponding author: R. K. Padmashini (padmashinirkeee@gmail.com)
DOI: https://doi.org/10.47738/jads.v7i3.1466

the stability of DC power systems in all-electric ships, particularly when transient power demand cannot be managed effectively by a single storage technology [4]. Nevertheless, the performance of the overall system depends not only on storage capacity but also on the ability of the power-management controller to coordinate PV generation, wind generation, battery operation, and propulsion demand in real time. Efficient power conversion represents another critical requirement because the low and variable voltage generated by renewable sources must be regulated before it can supply the propulsion drive. DC–DC converters provide the voltage-conditioning interface between the renewable sources and the common DC bus, while their dynamic characteristics determine the transient response, voltage gain, and stability of the system [5]. Accurate modelling of PV generation is also required because a substantial proportion of the available generation may be unmonitored or affected by rapidly changing operating conditions [6]. Although several high-gain and multi-output converter structures have been developed, conventional topologies may require additional semiconductor devices, introduce high component stress, or increase control complexity [7]. A high-gain single-switch SEPIC configuration is therefore considered in this study to provide continuous input current, increased voltage conversion gain, and simplified switching control.

The wind-energy conversion stage introduces additional control challenges because oscillations and disturbances generated on the AC side can propagate to the DC link through the rectification stage. Compensation and damping strategies have been developed to mitigate oscillatory behavior in DFIG-based wind farms [8]; however, a marine hybrid system also requires coordinated voltage regulation across multiple energy sources. A fixed-gain or conventionally tuned controller may not provide satisfactory performance across nonlinear and time-varying operating conditions. An adaptive neuro-fuzzy inference system (ANFIS) is suitable for this problem because it combines data-driven learning with fuzzy rule-based reasoning, enabling nonlinear relationships between voltage error, error variation, and control action to be represented. Its effectiveness, however, remains dependent on the selection of membership-function and consequent parameters.

At the load-side interface, a multilevel inverter is required to convert the regulated DC-link voltage into a high-quality AC supply for the three-phase induction motor. Cascaded H-bridge multilevel inverters can produce a staircase voltage waveform with lower harmonic distortion and reduced filtering requirements, but conventional symmetrical structures generally require a large number of isolated sources and switching devices. Reduced-switch symmetrical and asymmetrical configurations have consequently been investigated to increase the number of voltage levels while limiting the semiconductor count [9]. Renewable-source-fed multilevel inverter systems have further demonstrated the suitability of these structures for integrating variable DC sources with AC loads [10]. Recent reviews nevertheless identify device count, voltage-source arrangement, switching losses, voltage balancing, and control complexity as continuing design constraints in high-level inverter topologies [11].

To address these interconnected challenges, this study proposes a hybrid PV–wind–battery propulsion system incorporating a high-gain SEPIC converter, a PWM rectifier, a bidirectional battery converter, and a reduced-switch 31-level cascaded H-bridge inverter for a three-phase induction motor. A Lion Optimization Algorithm is employed to tune the ANFIS controller used for maximum power point tracking and DC-link voltage regulation. The proposed framework is designed to improve convergence, reduce steady-state error, maintain voltage stability under changing renewable inputs, and enhance the quality of the inverter output. Its performance is evaluated through simulation and experimental implementation by analyzing source-side responses, converter regulation, battery state of charge, inverter voltage and current, motor operation, and total harmonic distortion.

2. Literature Review

The integration of photovoltaic (PV), wind, and battery energy storage systems has been widely investigated to improve the reliability, continuity, and quality of renewable power generation. Hybrid wind–solar–battery architectures effectively mitigate the intermittent nature of renewable sources by combining complementary energy profiles with energy storage and advanced power conversion techniques [12]. Nevertheless, fluctuations in solar irradiance, ambient temperature, and wind speed continue to create highly nonlinear operating conditions that complicate maximum power extraction and DC-link voltage regulation. In PV systems, partial shading and module mismatch significantly reduce energy conversion efficiency unless adaptive control strategies are employed to continuously track the optimal operating point [13]. Likewise, wind energy conversion systems, particularly those based on doubly fed induction

ISSN 2723-6471

generators (DFIGs), are susceptible to grid disturbances and oscillatory dynamics that adversely affect output power stability [14].

To interface low-voltage renewable sources with medium- or high-voltage DC buses, high-voltage-gain DC–DC converters have become an essential component of modern renewable energy systems. Transformer less and switched-inductor converter topologies have demonstrated superior voltage gain while reducing the size, weight, and cost associated with conventional isolated converters [15]. However, achieving higher voltage conversion ratios generally requires additional semiconductor devices and passive components, resulting in increased conduction losses, switching complexity, and control challenges. Alternative converter topologies, including single-input multi-output and resonant converter structures, have been proposed to achieve high voltage gain with improved efficiency, although their performance remains dependent on switching frequency, component stress, source characteristics, and output regulation requirements [16]. Consequently, various closed-loop control and parameter tuning techniques have been developed to enhance converter transient response and maintain voltage stability under source and load disturbances [17].

To overcome the limitations of conventional fixed-parameter controllers, intelligent and adaptive control techniques have received increasing attention in renewable energy applications. Reinforcement learning integrated with sliding-mode control has demonstrated improved robustness in PV grid-connected systems operating under varying environmental and system conditions [18]. Another promising approach is the Adaptive Neuro-Fuzzy Inference System (ANFIS), which effectively models nonlinear input–output relationships through trainable fuzzy inference rules. Nevertheless, the performance of ANFIS strongly depends on the selection of membership functions, rule parameters, and training conditions. Therefore, optimization algorithms can be employed to determine optimal controller parameters that minimize tracking error, overshoot, settling time, and steady-state error. This motivates the integration of the Lion Optimization algorithm with ANFIS to achieve superior maximum power point tracking (MPPT) and DC-link voltage regulation compared with conventionally tuned intelligent controllers.

On the inverter side, multilevel inverter (MLI) topologies have become a preferred solution for renewable energy conversion and motor-drive applications because they generate high-quality AC waveforms with reduced voltage stress, lower harmonic distortion, and improved efficiency [19]. Advanced modulation techniques, particularly space-vector pulse-width modulation (SVPWM), have further enhanced voltage-vector utilization and switching-state optimization in multilevel converters [20]. Moreover, recent developments in reduced-switch and switched-inductor multilevel inverter structures have increased the number of output voltage levels while minimizing semiconductor count, making them attractive for high-performance induction motor drives and renewable energy systems [21]. Despite these advances, a comprehensive system that simultaneously integrates hybrid renewable energy sources, adaptive MPPT based on Lion Optimization–ANFIS, high-gain DC–DC conversion, coordinated battery energy storage, a reduced-switch 31-level inverter, and induction motor operation remains insufficiently investigated in the existing literature.

3. Methodology

3.1. Proposed System Architecture and Experimental Configuration

The proposed system integrates photovoltaic generation, wind generation, battery storage, DC–DC power conversion, a 31-level cascaded H-bridge multilevel inverter, and a three-phase induction motor (see figure 1). The PV array is connected to the common DC link through a high-gain SEPIC converter, whereas the wind energy conversion system uses a doubly fed induction generator followed by a PWM rectifier. A bidirectional DC–DC converter manages battery charging and discharging according to renewable-power availability and load demand. The regulated DC-link voltage is supplied to the reduced-switch 31-level cascaded H-bridge multilevel inverter, which generates the three-phase AC voltage required by the induction motor.

The Lion-optimized ANFIS controller regulates both renewable-source interfaces. At the PV interface, the controller adjusts the SEPIC converter duty cycle to track the maximum power point and maintain a stable converter output. At the wind interface, it controls the PWM rectifier to suppress voltage fluctuations caused by wind-speed variations. When the combined PV and wind generation is insufficient, the battery discharges to support the DC link. Conversely, excess renewable energy is directed to the battery charging process. This coordinated configuration follows the hybrid

ISSN 2723-6471

renewable-generation principle used in wind–solar–battery systems [19], while the high-gain conversion stage is designed to avoid the excessive device count associated with several conventional converter structures [13].

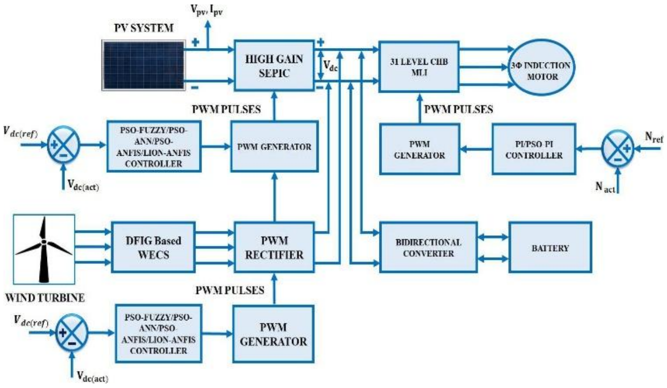

Figure 1. Proposed PV–wind–battery energy conversion and induction-motor drive architecture.

3.2. Mathematical Modelling and Lion-Optimized ANFIS Control

The PV array is represented using the single-diode model. The output current is expressed as:

$$I_{\text{PV}} = I_{\text{ph}} - I_0\left[\exp\left(\frac{V_{\text{PV}} + I_{\text{PV}}R_s}{aV_T}\right) - 1\right] - \frac{V_{\text{PV}} + I_{\text{PV}}R_s}{R_{\text{sh}}} \tag{1}$$

I_{ph} is the photocurrent, I0I_0I0 is the diode saturation current, R_s and R_{sh} are the series and shunt resistances, a is the diode ideality factor, and V_T is the thermal voltage. The generated PV power is calculated as $P_{\text{PV}} = V_{\text{PV}}I_{\text{PV}}$. The MPPT controller uses changes in PV voltage and power to determine the appropriate duty-cycle adjustment.

The proposed high-gain SEPIC converter operates in continuous conduction mode and contains three inductors, three capacitors, three diodes, and one controlled switch. During the switch-ON interval, the inductors store energy while the output capacitor supplies the load. During the switch-OFF interval, the stored inductor energy is transferred to the capacitors and DC link. Under ideal steady-state conditions, the converter voltage gain can be represented as:

$$G_{\text{SEPIC}} = \frac{V_{\text{dc}}}{V_{\text{PV}}} = \frac{1 + D}{1 - D} \tag{2}$$

D denotes the converter duty cycle. This relationship is used as the initial analytical basis, while the actual switching command is continuously adjusted by the Lion-ANFIS controller. The ANFIS controller receives two inputs: the voltage or power error and the change in error. For DC-link regulation, these inputs are formulated as:

$$e(k) = V_{\text{dc}}^* - V_{\text{dc}}(k), \qquad \Delta e(k) = e(k) - e(k-1) \tag{3}$$

V_{dc}^* is the reference DC-link voltage and $V_{\text{dc}}(k)$ is the measured voltage at sampling instant k. The ANFIS output is the incremental duty-cycle command $\Delta D(k)$. The controller consists of fuzzification, rule activation, normalized firing-strength calculation, consequent evaluation, and output aggregation. For a first-order Takagi–Sugeno rule, the controller output is written as:

$$u = \frac{\sum_{i=1}^{N_r} w_i(p_i e + q_i \Delta e + r_i)}{\sum_{i=1}^{N_r} w_i} \tag{4}$$

N_r is the number of fuzzy rules, w_i is the firing strength of rule i, and p_i, q_i, and r_i are consequent parameters. The Lion Optimization Algorithm is used to determine the ANFIS premise and consequent parameters. Each candidate lion represents one complete parameter vector. The population is divided into resident prides and nomadic lions, while candidate solutions are updated through hunting, roaming, mating, defense, and territorial replacement. The optimization minimizes a composite control objective defined as:

$$J = \alpha\,\text{IAE} + \beta\,t_s + \gamma\,M_p + \delta\,e_{ss}^2 \tag{5}$$

ISSN 2723-6471

IAE is the integral absolute error, t_s is the settling time, M_p is the maximum overshoot, and e_{ss} is the steady-state error. The weights α, β, γ, and δ determine the relative importance of each control criterion.

Figure 2 illustrates the complete workflow of the proposed Lion-optimized ANFIS controller, consisting of an offline training stage and an online execution stage. During offline training, measured variables, including PV voltage, PV current, wind-side voltage, and DC-link voltage, are used to calculate the controller inputs, namely the voltage error and change in error. The ANFIS structure is initialized with predefined membership functions, while each candidate solution in the Lion Optimization (LO) algorithm represents a complete set of ANFIS parameters. The optimization process evaluates each candidate using an objective function based on voltage regulation performance, followed by hunting, roaming, mating, and defense operations to update the population iteratively until the stopping criterion is satisfied. The optimized ANFIS parameters are then transferred to the online controller, where the trained ANFIS generates incremental duty-cycle commands in real time to regulate the SEPIC converter and PWM rectifier. This process is repeated at every sampling interval, enabling adaptive DC-link voltage regulation under continuously varying operating conditions.

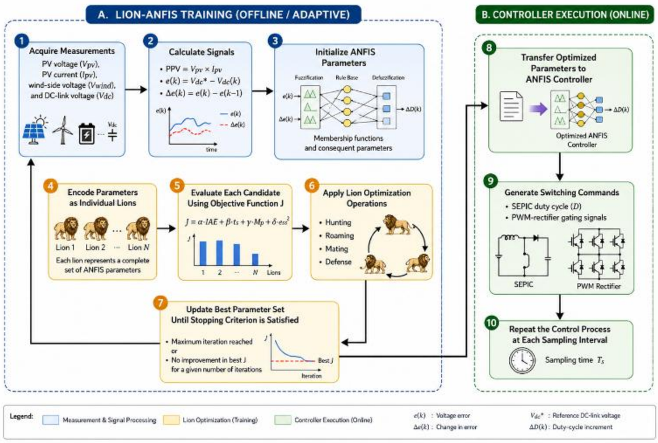

Figure 2. Training and execution workflow of the Lion-optimized ANFIS controller.

Table 1 summarizes the optimization settings adopted for the proposed Lion-ANFIS controller. A population of 30 lions is divided into four prides, with 20% of the population designated as nomadic lions and an 80% female ratio to preserve the natural social structure of the algorithm. The optimization is executed for a maximum of 100 iterations with a mating probability of 0.30 and an initial roaming ratio of 0.20, while the objective function is evaluated through 10 independent runs to improve solution robustness. The ANFIS controller uses the voltage error and change in error as input variables and produces an incremental duty-cycle command as its output. The optimization terminates when either the maximum number of iterations is reached or the best fitness value remains unchanged for 15 consecutive iterations, providing a balance between computational efficiency and convergence accuracy.

Table 1. Lion-ANFIS optimization settings

Parameter	Value
Population size	30 lions
Maximum iterations	100
Number of prides	4
Nomadic population ratio	20%
Female ratio	80%
Mating probability	0.30
Initial roaming ratio	0.20
Objective-function repetitions	10 independent runs
Controller inputs	Error and change in error
Controller output	Incremental duty-cycle command
Stopping criterion	Maximum iteration or unchanged best fitness for 15 iterations

3.3. Inverter Operation, Validation Procedure, and Performance Measures

The regulated DC-link voltage is converted into a three-phase AC output using the proposed reduced-switch 31-level cascaded H-bridge (CHB) inverter. The inverter consists of a switched-source multilevel stage and a conventional H-bridge output stage, enabling the generation of 31 discrete voltage levels while requiring fewer power semiconductor devices than conventional symmetric CHB topologies [22]. The switched-source stage synthesizes multiple voltage magnitudes from four unequal DC sources, whereas the H-bridge determines the polarity of the output voltage. This configuration reduces switching losses, gate-driver requirements, converter size, and implementation cost while maintaining high-quality output waveforms suitable for renewable-energy and motor-drive applications. The complete topology of the proposed inverter is illustrated in figure 3.

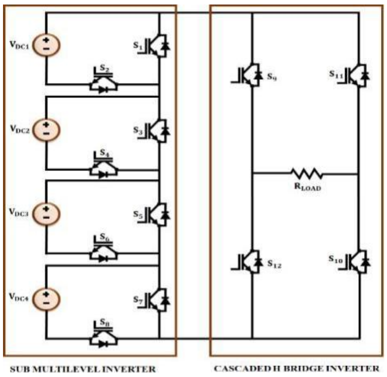

Figure 3. Reduced-switch 31-level cascaded H-bridge inverter topology.

As shown in Figure 3, switches S1–S8 are responsible for selecting the appropriate combination of DC voltage sources to produce the required voltage magnitude, while switches S9–S12 form the H-bridge that alternates the output polarity during positive and negative half cycles. During positive operation, switches H1 and H2 conduct while H3 and H4 remain off. Conversely, H3 and H4 conduct during the negative half cycle, producing the corresponding negative voltage levels. Zero output voltage is obtained by disabling the switching paths. This operating principle enables the synthesis of a staircase voltage waveform with significantly lower harmonic distortion than conventional two-level inverters. The switching combinations required to generate all 31 voltage levels are summarized in table 2.

Table 2. Switching states of the 31-level CHB inverter.

Inverter Output Voltage	(S_4)	(S_3)	(S_2)	(S_1)	(H_1)	(H_2)	(H_3)	(H_4)
$(15V_{dc})$	1	1	1	1	1	1	0	0
$(14V_{dc})$	1	1	1	0	1	1	0	0
$(13V_{dc})$	1	1	0	1	1	1	0	0
$(12V_{dc})$	1	1	0	0	1	1	0	0
$(11V_{dc})$	1	0	1	1	1	1	0	0
$(10V_{dc})$	1	0	1	0	1	1	0	0
$(9V_{dc})$	1	0	0	1	1	1	0	0
$(8V_{dc})$	1	0	0	0	1	1	0	0
$(7V_{dc})$	0	1	1	1	1	1	0	0
$(6V_{dc})$	0	1	1	0	1	1	0	0
$(5V_{dc})$	0	1	0	1	1	1	0	0
$(4V_{dc})$	0	1	0	0	1	1	0	0
$(3V_{dc})$	0	0	1	1	1	1	0	0
$(2V_{dc})$	0	0	1	0	1	1	0	0
$(1V_{dc})$	0	0	0	1	1	1	0	0
(0)	0	0	0	0	0	0	0	0
$(-1V_{dc})$	0	0	0	1	0	0	1	1

 ISSN 2723-6471

$(-2V_{dc})$	0	0	1	0	0	0	1	1
$(-3V_{dc})$	0	0	1	1	0	0	1	1
$(-4V_{dc})$	0	1	0	0	0	0	1	1
$(-5V_{dc})$	0	1	0	1	0	0	1	1
$(-6V_{dc})$	0	1	1	0	0	0	1	1
$(-7V_{dc})$	0	1	1	1	0	0	1	1
$(-8V_{dc})$	1	0	0	0	0	0	1	1
$(-9V_{dc})$	1	0	0	1	0	0	1	1
$(-10V_{dc})$	1	0	1	0	0	0	1	1
$(-11V_{dc})$	1	0	1	1	0	0	1	1
$(-12V_{dc})$	1	1	0	0	0	0	1	1
$(-13V_{dc})$	1	1	0	1	0	0	1	1
$(-14V_{dc})$	1	1	1	0	0	0	1	1
$(-15V_{dc})$	1	1	1	1	0	0	1	1

The proposed Lion-ANFIS controller is validated through both MATLAB/Simulink simulation and laboratory-scale hardware implementation. To comprehensively evaluate controller performance, eight operating scenarios are designed to represent steady-state operation, renewable-source disturbances, battery charging/discharging conditions, induction motor dynamics, and inverter power-quality assessment. These experimental scenarios and their corresponding evaluation objectives are summarized in table 3.

Table 3. Experimental scenarios and evaluation objectives

Scenario	Input condition	Evaluation objective
S1	Irradiance: 800 W/m²; temperature: 25 °C	Initial steady-state performance
S2	Irradiance step: 800 to 1000 W/m² at 0.3 s	MPPT transient response
S3	Temperature step: 25 to 35 °C at 0.3 s	Robustness against PV-temperature variation
S4	Variable DFIG output voltage	PWM-rectifier and DC-link regulation
S5	Renewable power below load demand	Battery discharging response
S6	Renewable power above load demand	Battery charging response
S7	Motor startup and rated-load operation	Speed, current, and torque response
S8	31-level inverter at steady state	RMS voltage, current, real power, reactive power, and THD

The simulation is conducted for 0.5 s. Solar irradiance is initially maintained at 800 W/m² and increased to 1000 W/m² at t = 0.3 s, while the PV module temperature simultaneously changes from 25 °C to 35 °C. These disturbances are introduced to evaluate the MPPT response, converter transient performance, and DC-link voltage regulation. Wind-side voltage variations are also applied to assess the robustness of the PWM rectifier controller. The battery energy storage system is initialized with a state of charge (SOC) of 60% and automatically operates in charging or discharging mode according to the instantaneous renewable power balance.

The hardware platform consists of an FPGA-based controller, a PV source (or PV emulator), a DFIG wind-source emulator, a high-gain SEPIC converter, a PWM rectifier, a bidirectional battery converter, the proposed reduced-switch 31-level inverter, and a three-phase induction motor. Voltage and current waveforms are acquired using a digital storage oscilloscope, while motor speed and battery variables are monitored through the embedded controller. The same DC-link reference voltage, switching frequency, inverter topology, and controller parameters used in the simulation are implemented during the hardware experiments to ensure a fair comparison.

4. Results and Discussion

4.1. Renewable-Source and DC-Link Performance

The dynamic performance of the proposed PV generation system was first evaluated under simultaneous variations in solar irradiance and cell temperature to examine the effectiveness of the Lion-ANFIS-based MPPT controller. Initially,

Journal of Applied Data Sciences
Vol. 7, No. 3, September 2026, pp. 2161-2174

the solar irradiance was maintained at 800 W/m², while the PV cell temperature was fixed at 25 °C. At t = 0.3 s, the irradiance was increased to 1000 W/m², and the temperature was simultaneously raised to 35 °C. These operating conditions were intentionally introduced to emulate realistic environmental variations and to assess the controller's ability to rapidly identify the new maximum power point while maintaining stable DC-link power delivery. The corresponding environmental inputs and PV electrical responses are presented in figure 4.

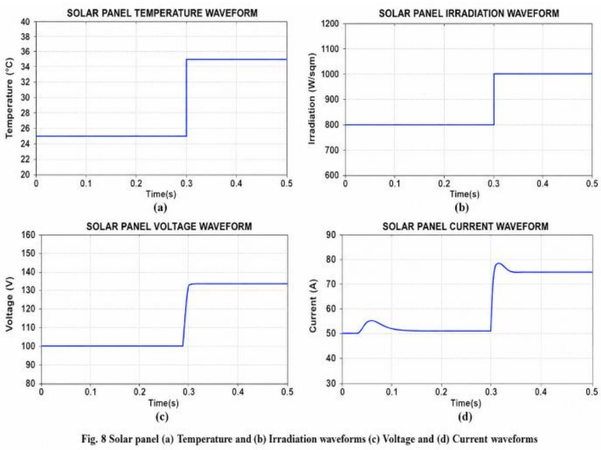

Figure 4. PV response under changes in temperature and solar irradiance: (a) temperature, (b) irradiance, (c) output voltage, and (d) output current.

As illustrated in figure 4(a) and figure 4(b), both the temperature and irradiance undergo step changes at 0.3 s, creating a new operating condition for the PV array. In response, the PV voltage shown in figure 4(c) increases rapidly from approximately 100 V to 134 V, reaching the new steady-state value with negligible overshoot and without noticeable oscillations. Similarly, the PV current in figure 4(d) rises from approximately 50 A to 75 A, exhibiting only a small transient before settling quickly to the desired operating point. The smooth voltage and current transitions indicate that the proposed Lion-ANFIS controller successfully tracks the new maximum power point despite the simultaneous increase in irradiance and temperature. Furthermore, the absence of sustained oscillations demonstrates effective suppression of steady-state tracking errors, thereby ensuring stable power extraction and providing a well-regulated DC-link voltage for the subsequent converter and inverter stages.

The voltage regulation capability of the high-gain SEPIC converter was subsequently evaluated by comparing four intelligent control strategies, namely PSO-Fuzzy, PSO-ANN, PSO-ANFIS, and the proposed Lion-ANFIS controller. The objective of this comparison was to investigate the influence of different optimization methods on converter transient performance and steady-state voltage regulation under identical operating conditions. The converter output-voltage responses obtained using each controller are presented in figure 5.

As shown in figure 5(a), the PSO-Fuzzy controller is capable of regulating the converter output to the 400 V reference; however, it exhibits a relatively large overshoot and noticeable oscillations before reaching steady-state operation. A similar transient behavior is observed for the PSO-ANN controller in figure 5(b), although the oscillation amplitude is slightly reduced. The PSO-ANFIS controller presented in figure 5(c) provides improved dynamic performance by decreasing both overshoot and settling time, resulting in a smoother convergence toward the reference voltage. Among all evaluated controllers, the proposed Lion-ANFIS controller in figure 5(d) demonstrates the best voltage regulation performance. The output voltage rapidly reaches the 400 V reference with the smallest overshoot, minimal transient oscillation, and the shortest settling time while maintaining a nearly ripple-free steady-state response.

he superior performance of the proposed controller is attributed to the Lion Optimization algorithm, which effectively determines the ANFIS membership-function parameters and consequent coefficients during the offline optimization stage. Consequently, the optimized controller provides more accurate control actions during transient operating conditions, improving DC-link voltage stability and reducing steady-state error. These characteristics are particularly advantageous for hybrid renewable-energy systems, where rapid variations in source power require fast and robust converter regulation to maintain stable operation of the downstream inverter and motor-drive system.

ISSN 2723-6471

The performance of the wind-energy conversion stage is evaluated next by analyzing the DFIG output characteristics and the corresponding PWM rectifier response, which converts the variable AC voltage into a regulated DC voltage before supplying the common DC-link.

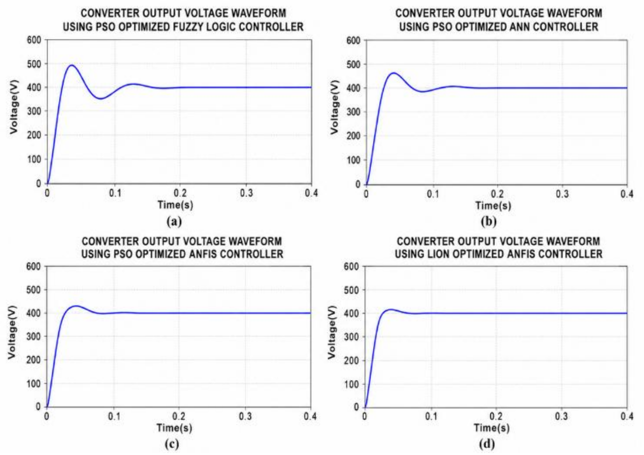

Figure 5. Converter output-voltage responses using (a) PSO-Fuzzy, (b) PSO-ANN, (c) PSO-ANFIS, and (d) Lion-ANFIS controllers.

The effectiveness of the proposed controller was further evaluated on the wind-energy conversion stage to verify its ability to regulate the DC-link voltage under fluctuating wind-source conditions. The variable AC voltage generated by the DFIG was first processed by the PWM rectifier before being supplied to the common DC-link shared with the PV generation system. This experiment was conducted to assess the capability of the rectifier-controller combination in rejecting source-side voltage variations and maintaining a stable DC-link voltage. The corresponding DFIG output voltage and PWM rectifier output voltage are presented in figure 6.

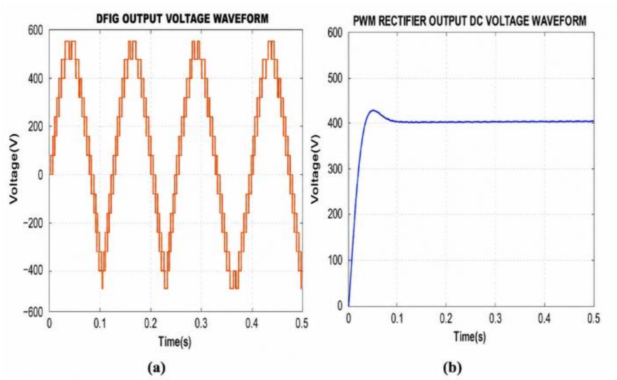

Figure 6. Wind-energy conversion response: (a) DFIG output voltage and (b) PWM-rectifier output voltage.

As illustrated in figure 6(a), the DFIG produces a variable AC voltage with continuously changing instantaneous values, representing the inherent fluctuations associated with wind-energy generation. After rectification and closed-loop regulation, the PWM rectifier successfully converts the variable AC input into a nearly constant DC output, as shown in figure 6(b). Although a small transient overshoot is observed during the initial start-up period, the output voltage rapidly converges to the 400 V reference with negligible steady-state ripple and without sustained oscillations. These results demonstrate that the proposed Lion-ANFIS controller effectively compensates for variations in the DFIG output, thereby preventing wind-induced disturbances from propagating to the common DC-link.

The coordinated regulation of the PV-side SEPIC converter and the wind-side PWM rectifier ensures that both renewable energy sources contribute stable DC power to the hybrid system despite their different electrical characteristics and operating conditions. Consequently, the downstream multilevel inverter and induction motor are supplied with a well-regulated DC-link voltage, improving overall system stability and dynamic performance. A summary of the renewable-source responses and DC-link regulation performance is presented in table 4.

Table 4. Summary of renewable-source and DC-link responses

Performance variable	Observed result
Initial PV irradiance	800 W/m²
Final PV irradiance	1000 W/m²
Initial PV temperature	25 °C
Final PV temperature	35 °C
Stabilized PV voltage	Approximately 134 V
Stabilized PV current	Approximately 75 A
SEPIC converter output	Approximately 400 V
PWM-rectifier output	Approximately 400 V
Best comparative controller	Lion-ANFIS
Steady-state behaviour	Stable with limited voltage fluctuation

4.2. Battery, Multilevel Inverter, and Motor-Side Performance

The performance of the battery energy storage system (BESS) was subsequently evaluated to verify its capability in balancing the instantaneous mismatch between renewable power generation and the induction-motor load demand. Through the bidirectional DC–DC converter, the battery operates in charging mode when the renewable generation exceeds the load requirement and automatically switches to discharging mode when the generated power becomes insufficient. This coordinated energy-management strategy is intended to maintain a stable DC-link voltage while minimizing unnecessary battery cycling. The corresponding battery voltage, current, and state-of-charge (SOC) responses are presented in figure 7.

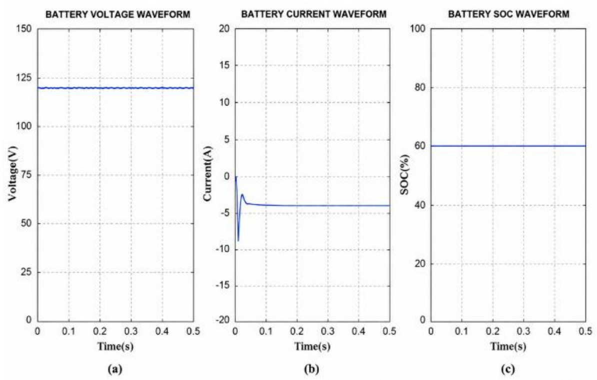

Figure 7. Battery operating response: (a) voltage, (b) current, and (c) state of charge.

As illustrated in figure 7(a), the battery voltage remains nearly constant at approximately 120 V throughout the simulation, indicating stable operation of the bidirectional converter. The battery current shown in figure 7(b) exhibits only a short transient during the initial operating period before settling to a nearly constant value, demonstrating smooth power exchange between the battery and the DC-link. Meanwhile, the SOC profile in figure 7(c) remains close to 60% with negligible variation, confirming that the proposed energy-management strategy successfully prevents excessive charging and discharging cycles. Maintaining the battery near its nominal SOC provides sufficient operating margin for both charging and discharging events, thereby improving battery lifetime while ensuring continuous support during renewable-power fluctuations.

The regulated DC-link voltage is subsequently supplied to the proposed reduced-switch 31-level cascaded H-bridge inverter to generate the three-phase AC voltage required by the induction motor. The objective of this stage is to evaluate the inverter output quality and its capability to deliver a stable voltage and current under steady-state operation. The simulated output voltage and current waveforms of the 31-level inverter are presented in figure 8.

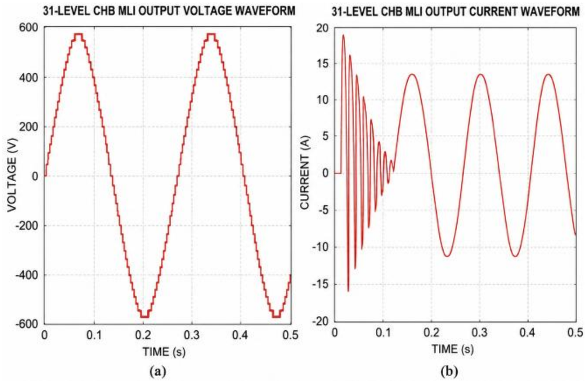

Figure 8. Simulated 31-level inverter output: (a) voltage waveform and (b) current waveform.

As shown in figure 8(a), the inverter successfully synthesizes the expected 31-level staircase voltage waveform, closely approximating a sinusoidal waveform through multiple discrete voltage levels. Compared with conventional two-level inverters, the smaller voltage steps significantly reduce waveform distortion and switching stress. The output voltage reaches a peak value of approximately ±600 V, while the output current shown in figure 8(b) exhibits a short start-up transient before settling to approximately 14 A after 0.2 s. The absence of sustained oscillations in the steady-state current demonstrates that the inverter provides a stable supply for the induction-motor load. To further evaluate the quality of power delivered to the load, the RMS output voltage, converter output current, real power, and reactive power were monitored throughout the simulation. These responses are presented in figure 9.

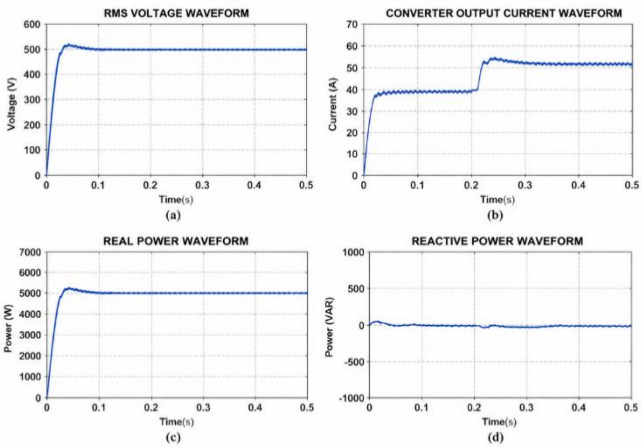

Figure 9. Simulated inverter and load responses: (a) RMS voltage, (b) converter current, (c) real power, and (d) reactive power.

As illustrated in figure 9(a), the RMS output voltage rapidly increases during start-up and stabilizes at approximately 499 V within 0.1 s, indicating effective voltage regulation by the proposed converter–inverter system. The converter output current shown in figure 9(b) follows the load demand with only minor transient variations before reaching steady-state operation. Likewise, the real power in figure 9(c) converges to approximately 4.99 kW, while the reactive power presented in figure 9(d) remains comparatively small and exhibits only slight fluctuations around the steady-state operating point. These results confirm that the proposed hybrid renewable-energy system delivers stable active power while maintaining a low reactive-power demand, thereby improving the overall efficiency of the power conversion process. The output voltage quality of the proposed multilevel inverter was finally evaluated through harmonic analysis. The corresponding harmonic spectrum is shown in figure 10.

As shown in Figure 10, the fundamental output frequency is 50 Hz, and the total harmonic distortion (THD) is limited to only 1.39%, which is well below the 5% limit recommended by IEEE Std. 519 for voltage harmonic distortion. The low THD is primarily attributed to the 31-level voltage synthesis, which substantially reduces the difference between the staircase output waveform and the ideal sinusoidal reference. Consequently, the proposed inverter minimizes harmonic currents supplied to the induction motor, thereby reducing copper losses, torque ripple, electromagnetic vibration, and acoustic noise while improving the overall power quality of the drive system.

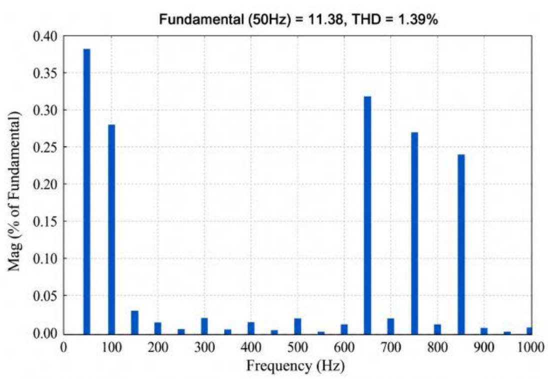

Figure 10. Harmonic spectrum of the simulated 31-level inverter output.

The overall simulation results demonstrate that the proposed Lion-ANFIS-controlled hybrid renewable-energy system provides stable battery operation, effective DC-link voltage regulation, high-quality multilevel voltage generation, and low harmonic distortion under varying renewable-energy operating conditions. A summary of the principal battery, inverter, and load-side performance indicators is provided in table 5.

Table 5. Simulated battery, inverter, and load-side performance

Performance variable	Observed result
Battery state of charge	Approximately 60%
Inverter output-voltage magnitude	Approximately 600 V
Steady-state output current	Approximately 14 A
RMS output voltage	Approximately 499 V
Real power	Approximately 4990 W
Simulated THD	1.39%
Induction-motor rated power	1 hp
Induction-motor rated speed	1390 rpm
Induction-motor rated voltage	415 V AC

5. Conclusion

This study developed and experimentally validated a hybrid PV–wind–battery energy conversion system for driving a three-phase induction motor. The proposed configuration combines a high-gain SEPIC converter, a PWM rectifier, a bidirectional battery converter, a Lion-optimized ANFIS controller, and a reduced-switch 31-level cascaded H-bridge inverter. The controller was designed to coordinate maximum power extraction and DC-link voltage regulation under changing solar irradiance, PV temperature, and wind-generation conditions.

The simulation results showed that the PV-side voltage and current stabilized at approximately 134 V and 75 A, while both the SEPIC converter and PWM rectifier maintained the common DC-link voltage near 400 V. The battery state of charge remained around 60%, indicating balanced charging and discharging operation. On the load side, the 31-level inverter produced an output-voltage magnitude of approximately 600 V, an RMS voltage of approximately 499 V, and real power of approximately 4990 W. The simulated inverter total harmonic distortion was limited to 1.39%.

Experimental validation confirmed the principal characteristics observed in the simulation. The prototype increased the PV input from approximately 130 V to a regulated output of approximately 400 V, stabilized the rectified wind-side voltage, and maintained the battery state of charge near 60%. The measured inverter THD was 2.85%, which remained low despite practical effects such as switching delays, semiconductor voltage drops, parasitic elements, component tolerances, and measurement noise. The close agreement between the simulated and experimental responses demonstrates the technical feasibility of the proposed control and power-conversion architecture.

Overall, the Lion-optimized ANFIS controller provided stable renewable-source integration, effective DC-link regulation, and improved transient behaviour compared with the evaluated PSO-based controllers. The reduced-switch

ISSN 2723-6471

31-level inverter also supplied the induction motor with a stable multilevel waveform and limited harmonic distortion. Future work should evaluate the system under longer operating periods, wider load and environmental variations, battery-aging conditions, and real-time marine propulsion duty cycles. Further investigation should also consider multi-objective controller optimization that simultaneously minimizes tracking error, converter losses, battery degradation, switching stress, and harmonic distortion.

6. Declarations

6.1. Author Contributions

Conceptualization: R.K.P., J.N.R.K.; Methodology: R.K.P., D.L.; Software: J.N.R.K., P.J.; Validation: D.L., C.N.R.; Formal Analysis: R.K.P.; Investigation: J.N.R.K., P.J.; Resources: D.L., C.N.R.; Data Curation: J.N.R.K.; Writing – Original Draft Preparation: R.K.P.; Writing – Review and Editing: D.L., P.J.; Visualization: P.J.; All authors have read and agreed to the published version of the manuscript.

6.2. Data Availability Statement

The data presented in this study are available on request from the corresponding author.

6.3. Funding

The authors received no financial support for the research, authorship, and/or publication of this article.

6.4. Institutional Review Board Statement

Not applicable.

6.5. Informed Consent Statement

Not applicable.

6.6. Declaration of Competing Interest

The authors declare that they have no known competing financial interests or personal relationships that could have appeared to influence the work reported in this paper.

References

[1] J. Liu, C. Jiang, J. He, Z. Tang, Y. Xie, and P. Xu, "STA-APSNFIS: STA-optimized adaptive pre-sparse neuro-fuzzy inference system for online soft sensor modeling," *IEEE Access*, vol. 8, pp. 104870–104883, Jun. 2020, doi: 10.1109/ACCESS.2020.2998792.

[2] B. Bilal, K. H. Adjallah, A. Sava, K. Yetilmezsoy, and E. Kıyan, "Wind power conversion system model identification using adaptive neuro-fuzzy inference systems: A case study," *Energy*, vol. 239, no. 1, pp. 1–19, Jan. 2022, doi: 10.1016/j.energy.2021.122089.

[3] B. Veluchamy, N. Karthikeyan, B. R. Krishnan, and C. M. Sundaram, "Surface roughness accuracy prediction in turning of Al7075 by adaptive neuro-fuzzy inference system," *Materials Today: Proceedings*, vol. 37, no. 6, pp. 1356–1358, Jan. 2021, doi: 10.1016/j.matpr.2020.06.560.

[4] K. M. Y. Acosta and R. G. Baldovino, "Predicting acute aquatic toxicity towards fathead minnow (Pimephales promelas) using neuro-fuzzy inference system (ANFIS)," *ICITEE*, vol. 2020, no. Oct., pp. 329–332, 2020, doi: 10.1109/ICITEE49829.2020.9271739.

[5] J. George and G. Mani, "A portrayal of sliding mode control through adaptive neuro-fuzzy inference system with optimization perspective," *IEEE Access*, vol. 12, pp. 3222–3239, Jan. 2024, doi: 10.1109/ACCESS.2023.3348836.

[6] V. V. Ignatyev, U. Tudevdagva, A. V. Kovalev, O. B. Spiridonov, A. V. Maksimov, and A. S. Ignatyeva, "Model of adaptive system of neuro-fuzzy inference based on PID- and PID-fuzzy-controllers," *Advances in Intelligent Systems and Computing*, vol. 2020, no. Aug., pp. 519–533, Aug. 2020, doi: 10.1007/978-3-030-51971-1_43.

[7] S. Mahato, S. Paul, N. Goyal, S. N. Mohanty, and S. Jain, "3EDANFIS: Three channel EEG-based depression detection technique with hybrid adaptive neuro-fuzzy inference system," *Recent Patents on Engineering*, vol. 17, no. 6, pp. 32–48, Aug. 2022, doi: 10.2174/1872212117666220801105612.

[8] A. Timene, N. Ngasop, and H. Djalo, "Tractor-implement tillage depth control using adaptive neuro-fuzzy inference system (ANFIS)," *Proceedings of Engineering and Technology Innovation*, vol. 19, no. May, pp. 53–61, May 2021, doi: 10.46604/peti.2021.7522.

[9] H. B. Nafea, Z. A. Aboelezz, and F. W. Zaki, "Quality of service (QoS) for LTE network based on adaptive neuro-fuzzy inference system," *IET Communications*, vol. 15, no. 5, pp. 683–694, Mar. 2021, doi: 10.1049/cmu2.12099.

[10] M. P. S. Kumar and K. M. Bee, "GLCM based cardiac fat segmentation on CT images using co-adaptive neuro-fuzzy inference system (CANFIS) classifier in comparison with adaptive neuro-fuzzy inference system (ANFIS) classifier," *AIP Conference Proceedings*, vol. 2023, no. Sep., pp. 1–8, Sep. 2023, doi: 10.1063/5.0151567.

[11] D. Marisno, C. S. Chin, C. Shan, and S. See, "Performance of adaptive neuro-fuzzy inference system state-of-charge estimation of lithium-ion batteries for electric ship," *ICCIA*, vol. 2023, no. Jun., pp. 205–209, Jun. 2023, doi: 10.1109/ICCIA59741.2023.00044.

[12] E. Dokur, U. Yuzgec, and M. Kurban, "Performance comparison of hybrid neuro-fuzzy models using meta-heuristic algorithms for short-term wind speed forecasting," *Electrica*, vol. 21, no. 3, pp. 305–321, Nov. 2021, doi: 10.5152/electrica.2021.21042.

[13] P. Juijerm, L. Angkurarach, and P. Naemchanthara, "Direct current field enhanced boronizing of stainless steels and predictive performance of diffusion kinetics, deep neural network, and adaptive neuro-fuzzy inference system on boride layer thickness," *J. Mater. Sci.*, vol. 58, no. 42, pp. 16507–16522, Oct. 2023, doi: 10.1007/s10853-023-09072-4.

[14] F. E. T. Munsayac *et al.*, "Detecting and locating brain tumors in magnetic resonance imaging (MRI) using an adaptive neuro-fuzzy inference system (ANFIS)," *TENCON*, vol. 2022, no. Nov., pp. 1–6, Nov. 2022, doi: 10.1109/TENCON55691.2022.9977901.

[15] G. Casalino, G. Castellano, and G. Zaza, "Using an adaptive neuro-fuzzy inference system for the classification of hypertension," *CEUR Workshop Proceedings*, vol. 2021, no. Sep., pp. 1–6, Sep. 2021.

[16] L. Qi, L. Zhao, Y. Fu, Z. Liu, and X. Li, "Evaluation of motivation factors of social work organizations with neuro-fuzzy inference system," *Advances in Transdisciplinary Engineering*, vol. 2022, no. Nov., pp. 992–997, Nov. 2022, doi: 10.3233/ATDE221124.

[17] N. Mondal, M. C. Mandal, B. Dey, and S. Das, "Genetic algorithm-based drilling burr minimization using adaptive neuro-fuzzy inference system and support vector regression," *Proc. Inst. Mech. Eng., Part B: J. Eng. Manuf.*, vol. 234, no. 5, pp. 956–968, Mar. 2020, doi: 10.1177/0954405419889183.

[18] F. M. P. Santos, A. Gonçalves, J. M. C. Sousa, and S. M. Vieira, "Distilling knowledge from deep neural networks to neuro-fuzzy inference systems," *IEEE Int. Conf. Fuzzy Syst.*, vol. 2025, no. Jun., pp. 1–6, Jun. 2025, doi: 10.1109/FUZZ62266.2025.11152050.

[19] M. Nazerian, F. Naderi, A. Partovinia, A. N. Papadopoulos, and H. Younesi-Kordkheili, "Developing adaptive neuro-fuzzy inference system-based models to predict the bending strength of polyurethane foam-cored sandwich panels," *Proc. Inst. Mech. Eng., Part L: J. Mater. Des. Appl.*, vol. 236, no. 1, pp. 3–22, Jan. 2022, doi: 10.1177/14644207211024278.

[20] Z. Yu, H. Du, Y. Lei, and M. Shan, "Short-term load forecasting of power system based on weighted improved adaptive neuro-fuzzy inference system and random forest," *IEEE Int. Conf. Power Sci. Technol.*, vol. 2024, no. Jul., pp. 2024–2029, Jul. 2024, doi: 10.1109/ICPST61417.2024.10601995.

[21] M. Jalal, P. Arabali, Z. Grasley, and J. W. Bullard, "Application of adaptive neuro-fuzzy inference system for strength prediction of rubberized concrete containing silica fume and zeolite," *Proc. Inst. Mech. Eng., Part L: J. Mater. Des. Appl.*, vol. 234, no. 3, pp. 438–451, Mar. 2020, doi: 10.1177/1464420719890370.

[22] S. Nugroho, D. F. Fitriyana, R. Ismail, T. A. Nurcholis, T. Cionita, and J. P. Siregar, "The effect of surface hardening on the HQ 705 steel camshaft using static induction hardening and tempering method," *Automotive Experiences*, vol. 5, no. 3, pp. 343–354, Sep. 2022.